Grain size effect on corrosion behavior of Inconel 625 film against molten MgCl2-NaCl-KCl salt

Jinghua Feng[a], Li Mao[a], Guangcui Yuan[b,c], Youyang Zhao[d], Judith Vidal[d], and Li (Emily) Liu[a]

[a] Rensselaer Polytechnic Institute, 110 8th St, Troy, NY 12180, USA
[b] NIST Center for Neutron Research, National Institute of Standards and Technology, Gaithersburg, MD 20899, USA
[c] Department of Physics, Georgetown University, Washington, DC 20057, USA
[d] National Renewable Energy Laboratory, Golden, CO 80401, USA

Highlights

- Grain size of Inconel 625 films grows with rising deposition temperature.
- Larger grain size Inconel 625 possesses better corrosion performance.
- Cr depletion is alleviated by increasing the grain size.
- K and Na are only observed in the smallest grain size Inconel.

Abstract

This study evaluated the grain size effect of Inconel 625 film against molten chloride salt. It is found that larger grain size Inconel 625 exhibits better corrosion resistance by reducing Cr depletion. ~ 2 nm surface NiO layer of Inconel 625 is incapable of compensating the negative effects from more initiation corrosion sites. Mo is the least likely leached element and its enrichment occurs in Cr-depleted regions as a result of Mo diffusion. Mg and Cl are two most seen salt elements in all corroded samples, while K and Na only attack Inconel 625 with the smallest grain size.

1. Introduction

Solar energy is considered to be one of the most promising green and renewable energy resources to replace fossil fuels [1]. It converts the sunlight energy into electricity by either photovoltaic (PV) panels or concentrated solar power (CSP) [2], [3]. CSP system is the more attractive option for large scale power generation as it overcomes the intermittency issues of PV using its thermal energy storage systems to balance supply and demand [4], [5]. Heat transfer fluid (HTF) is one of the most important components of CSP systems as it serves as both the heat transfer media and thermal energy storage (TES) media. Molten chloride salts are promising HTF candidates for new generation CSP benefiting from their high decomposition temperatures, good thermal properties and low cost [6]. But molten chloride salts are very corrosive thus highly corrosion resistant material is required for thermal components such as piping, storage tanks, and heat exchangers.

Pursuant to the DOE Public Access Plan, this document represents the authors' peer-reviewed, accepted manuscript. The published version of the article is available from the relevant publisher.

Inconel 625 is a Ni-based alloy strengthened mainly by the additions of carbon, molybdenum and niobium in a nickel-chromium matrix [7]. Its exceptional mechanical properties [8] and excellent corrosion resistance make it of special interest in numerous applications [9], [10]. However, the high cost of wrought Inconel 625 has largely impeded its industrial applications. Therefore, Inconel 625 coatings have been developed with lower cost while maintaining desired surface properties. Nowadays, Inconel 625 coatings are widely used to improve the corrosion performance of material surface [11].

In spite of excellent corrosion performance in a variety of applications, Inconel 625 film is still not good enough to withstand the corrosion from molten chloride salts. Previous studies have indicated that corrosion rates of the chloride salts to Inconel 625 are typically greater than 100 μm/year [12], which is not capable of meeting the next generation CSP requirement [13]. Corrosion resistance can be influenced by many factors such as grain size, surface morphology, texture, etc. To further improve corrosion performance of Inconel 625 film, it is critical to investigate the effects of those factors for Inconel 625 film in molten salt.

Grain size has been considered as a crucial factor affecting the corrosion properties of coatings. There has been extensive research on the effect of grain size on corrosion resistance of coatings [14], [15], [16], [17], [18], [19]. However, the results are inconsistent in those reports: the rise of grain size can lead to either increased or decreased corrosion resistance, varying among films and corrosion environments. For instance, Zamanzad-Ghavidel et al. found that the Ni coating with higher grain size is more corrosion resistant against 3.5% NaCl solutions [15]. On the contrary, Liu et al. reported that Ni-based alloy coating with smaller grain is less susceptible to corrosion in 0.5 M NaCl + 0.05 M H2SO4 acidic solution [17].

Thus, it is difficult to predict the grain size effect on the corrosion behavior of coatings. To date there has been relatively little research on the grain size effect of Inconel 625 coatings on its corrosion resistance to molten chloride salts. The goal of this study is to explore the microstructure of Inconel 625 film with different grain size and evaluate the grain size effect on the corrosion behavior of Inconel 625 film in ternary molten salt MgCl2-NaCl-KCl. The obtained results are helpful to improve the corrosion resistance of Inconel 625 film that could be used in new generation CSP.

2. Material and methods

2.1. Magnetron sputtering

~ 240 nm thick Inconel 625 alloy film deposited on sapphire (A-plane, Ra < 0.5 nm) were prepared by AJA Orion RF/DC magnetron Sputtering System. The Inconel 625 target installed in the sputtering system is supplied by Plasmaterials Inc and its chemical composition is listed in Table 1 below. The substrate bias voltage was set at − 93 V (5 W) while the target voltage was measured at about 355 V (95 W DC power). The substrate temperature was ranged from 15 to 600 °C to obtain films with varying grain size. The deposition working distance (between substrate and target) was about 20 cm.

Pursuant to the DOE Public Access Plan, this document represents the authors' peer-reviewed, accepted manuscript. The published version of the article is available from the relevant publisher.

Table 1. Main chemical composition of Inconel 625 sputtering target in this study.

Element	Ni	Cr	Mo	Fe	Nb+Ta	Co	Mn
wt%	58–71	21–23	8–10	5	3.2–3.8	1 max.	0.5 max.

2.2. Scanning electron microscope and energy-dispersive X-ray spectroscopy

The surface and cross-section of the specimen were examined by FEI VERSA 3D Dual Beam Scanning Electron Microscope. Images of the top surface morphology and cross-section of the Inconel film were taken using secondary electron mode at 20 kV. Focused ion beam (FIB) was applied to cut a cross section perpendicular to the surface. The sample stage was tilted to 52° before performing FIB cutting. Two protective layers (electron beam induced platinum film and ion-beam assisted platinum film) were deposited first to protect the Inconel film against the ion beam damage during the cutting [20].

Energy-dispersive X-ray Spectroscopy (EDS) in VERSA was used to measure the compositions and elemental distribution of the Inconel 625 films. The accelerating voltage of 12 kV was applied to the electron beam and the objective aperture size was set to 50 µm. The working distance was 12 mm. Quantitative microanalysis was carried out with ZAF correction provided by Aztec software.

2.3. X-ray reflectometry

X-ray Reflectometry (XRR) is an analytical technique for the investigation of the surface properties of materials. It allows characterization of thin layered structures and interfaces in materials using X-rays to probe the scattering length density (SLD) profile perpendicular to the surface and thereby obtain information about the surface roughness, thin film thickness, composition and density [21]. X-ray reflectometer with Cu Kα irradiation at National Institute of Standards and Technology (NIST) was used to measure the properties of the Inconel film. The slit opening (filter) was set to 12 mm in width (w) by 0.1 mm in height (h), allowing the tool to examine the Inconel film with spot size of $w \cdot (h/\sin\theta)$.

2.4. X-ray diffraction

X-ray diffraction (XRD) analysis was conducted via Bruker D8-Discover system with Cu Kα irradiation with power of 1.6 kW (40 kV and 40 mA). The system was employed in Bragg-Brentano geometry equipped with a four-bounce germanium incident beam monochromator and a three-bounce germanium diffracted beam monochromator. The XRD scan was ranged from 3 to 110 degrees with step size of 0.1 degree at rate of 1.2 s/step.

2.5. Corrosion test

Glove box (UNIlab pro) from MBRAUN with argon atmosphere was used to conduct corrosion test. A small benchtop muffle furnace FB1315M from Thermo Fisher Scientific is placed in the

Pursuant to the DOE Public Access Plan, this document represents the authors' peer-reviewed, accepted manuscript. The published version of the article is available from the relevant publisher.

glove box, with heating temperature range from 100 to 1100 °C, which covers the desired molten salt corrosion test temperature range from 550 to 650 °C. The ternary salt provided by National Renewable Energy Laboratory (NREL) with mol.%: 44.7 $MgCl_2$ - 25.8 KCl - 29.4 NaCl (corresponding to wt%: 53.9 $MgCl_2$ - 24.3 KCl - 21.8 NaCl) was used as the molten salt for the corrosion test, with the melting and solidification point of 385 °C ± 1 °C. The ternary salt was loaded in the alumina molten salt cell and then placed in the furnace. The heating and cooling rate was set to 4 °C/min to protect the alumina crucible. The corrosion test was conducted at three different temperatures (550, 600and650°C) for 30 min in the glove box with O_2 level < 10 ppm and H_2O level < 2 ppm.

3. Results

3.1. Characterization of Inconel 625 film

3.1.1. Surface morphology by SEM

Fig. 1 shows the SEM images at the same scale (~ 500 nm) of Inconel 625 coatings with different deposition temperature. All films display fine homogeneous structure overall. The grain size of the films, which is measured by Heyn's mean lineal intercept approach, grows with the rising deposition temperature (16.7 nm, 37.5 nm, 44.1 nm, 76.9 nm and 136.4 nm for coatings with deposition temperature of 15 °C, 150 °C, 300 °C, 450 °C, and 600 °C respectively).

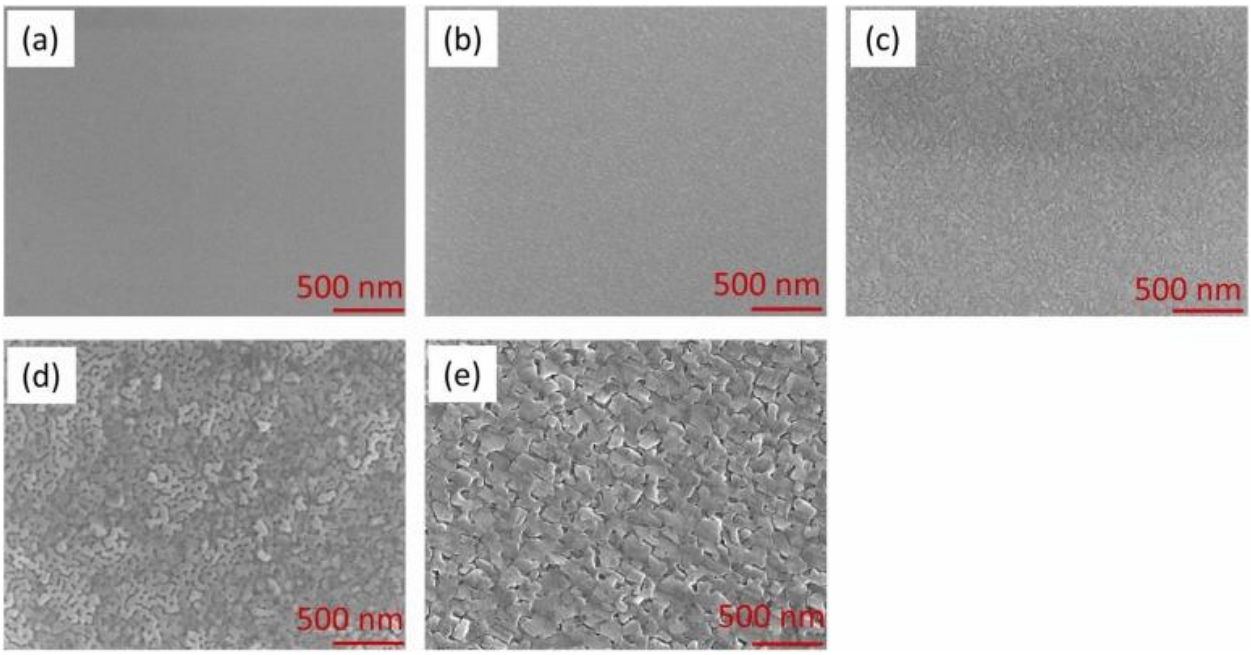

Fig. 1. SEM micrograph of Inconel 625 films deposited at different substrate temperatures: (a) 15 °C, (b) 150 °C, (c) 300 °C, (d) 450 °C and (e) 600 °C.

3.1.2. Crystallinity investigation by XRD

Pursuant to the DOE Public Access Plan, this document represents the authors' peer-reviewed, accepted manuscript. The published version of the article is available from the relevant publisher.

Fig. 2 exhibits the XRD ω-scan rocking curves of the (111) peak of Ni3Cr2 in Inconel 625 coatings deposited at different temperatures. The full width at half maximum (FWHM) values of the samples are around 16.90°, 18.51°, 4.31°, 4.33°, and 5.25° for films deposited at temperatures of 15°C, 150°C, 300°C, 450°C, and 600°C respectively, which indicates that film deposited at higher temperature has relatively higher degree of crystallinity.

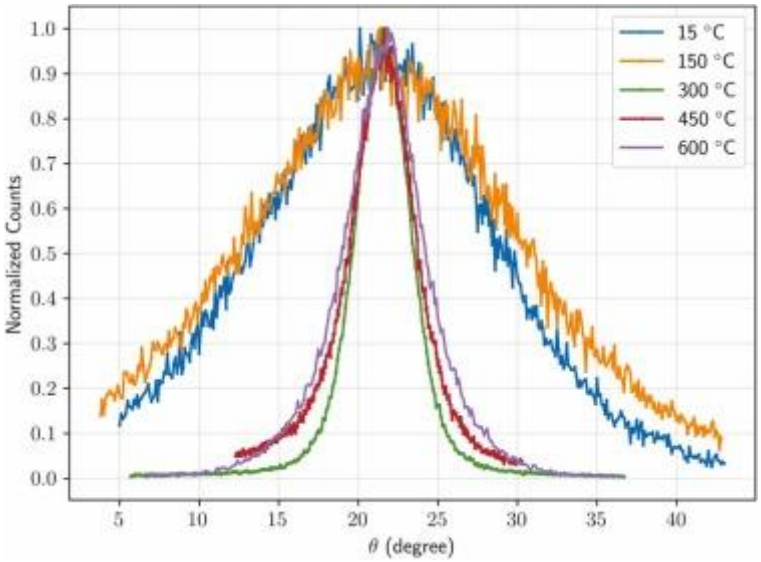

Fig. 2. Rocking curves of the (111) peak of Ni3Cr2 of Inconel 625 coatings deposited at different temperature.

3.1.3. Oxide measurement by XRR

The films deposited at 15 °C, 150 °C, 300 °C, 450 °C, and 600 °C for 30 min are all scanned by X-ray reflectometry (XRR) technique. The multilayer model developed in our previous work [22] was applied to evaluate the layered structure of the films, particularly the surface thin oxidation layer, which may play a key role against the corrosion. We used Refl1d program to fit the parameters (thickness, SLD, roughness, etc.) of reflectivity data with pre-defined hyperparameters (such as the model, learning algorithm, loss function, etc.). To yield a good fit without overfitting, normalized χ2 method is leveraged to evaluate the goodness of fit. We started with a base model Sapphire-Inconel 625-Air (three indispensable layers) and added physically realistic layers to obtain a good fit.

The optimal fitted results are displayed in Fig. 3, which indicates that there exists an oxide layer on top of Inconel films for grain size of 16.7 nm and 37.5 nm with thicknesses of 2.3 nm and 1.6 nm respectively, while no obvious oxidation is observed for the rest three films. The oxide layer is identified as NiO based on their SLD values.

Pursuant to the DOE Public Access Plan, this document represents the authors' peer-reviewed, accepted manuscript.
The published version of the article is available from the relevant publisher.

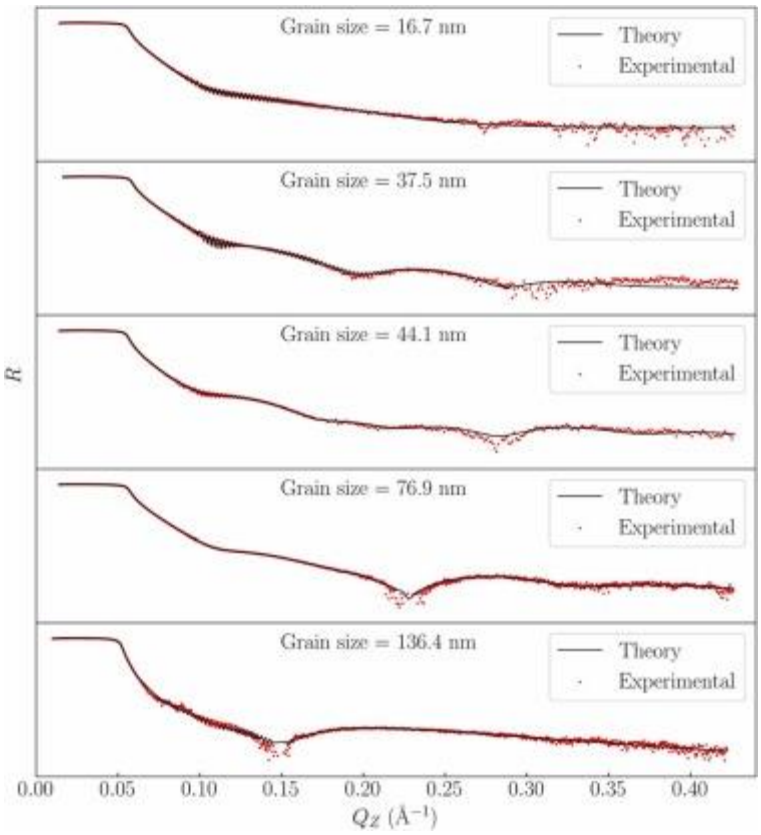

Fig. 3. Fitted XRR spectrums of Inconel 625 films with different grain size.

3.2. Corrosion results

To evaluate the grain size effect, we conducted three corrosion tests for the five films with different grain size at three different corrosion temperatures (550 °C, 600 °C, and 650 °C). At each test, five samples with different grain size are immersed in the same molten salt with the same duration. The images of the corroded samples are shown in Fig. 4. At 550 °C, samples display relatively less corrosion compared with those corroded at higher temperatures. At 650 °C, three films with smaller grain size completely peel off from the substrate after the corrosion test, while films with grain size of 76.9 nm and 136.4 nm survives after the test.

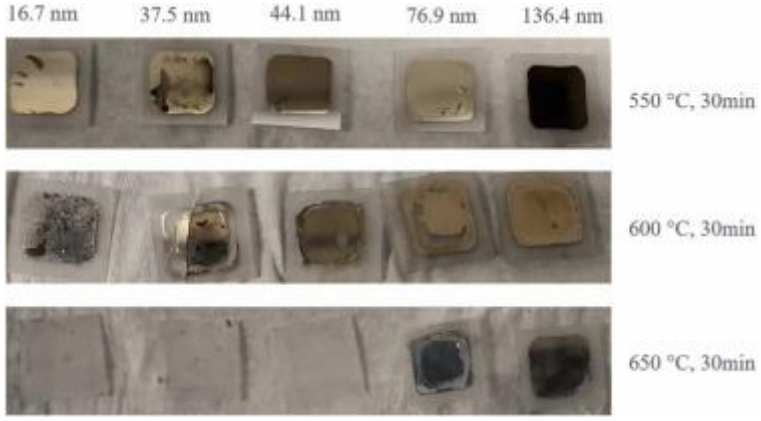

Pursuant to the DOE Public Access Plan, this document represents the authors' peer-reviewed, accepted manuscript.
The published version of the article is available from the relevant publisher.

Fig. 4. Images of corroded samples at different corrosion temperatures: grain size is listed in the first row, corrosion temperature and time are listed in the last column.

We conducted SEM and EDS analysis for the samples (Grain 16.7 nm, Corrosion 600 °C), (Grain 37.5 nm, Corrosion 600 °C), and (Grain 136.4 nm, Corrosion 600 °C) to further study the grain size effect. In addition, samples (Grain 136.4 nm, Corrosion 550 °C) and (Grain 136.4 nm, Corrosion 650 °C) are also studied to evaluate the influence of corrosion temperature.

3.2.1. Cross section surface analysis by SEM + FIB

To observe the effect of the growing grain size on corrosion resistance, we cut the films by Focused Ion Beam and observed the cross section morphology of the films by SEM. For comparison, the sample without corrosion is scanned as displayed in Fig. 5. Gallium ion beam is focused to cut a cross section along the vertical direction. But direct cutting by ion beam may cause damage to the Inconel film, thus two protective layers, ion-beam assisted and electron beam induced platinum films are deposited on top of the film [20], as shown in Fig. 5.

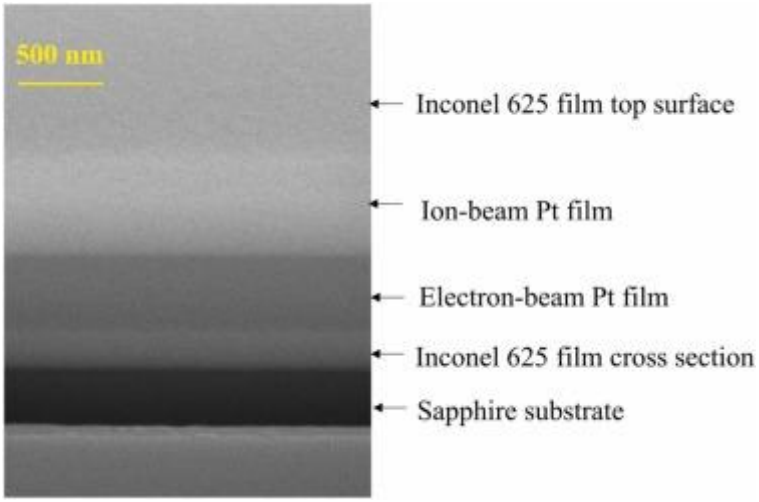

Fig. 5. Cross sections morphology of film deposited at 15 °C without corrosion.

The cross sections of corroded samples are illustrated in Fig. 6. Compared with the original film without corrosion, the sample with grain size of 16.7 nm after corrosion exhibits a large number of small corrosion sites throughout the film. For the sample with grain size of 37.5 nm, the number of pits decreases and most pits concentrates at the upper part of the film. When the grain size reaches to 136.4 nm, the number of pits further reduces although there exists some large size of pits. Overall, the film with larger grain size displays more corrosion resistant.

Pursuant to the DOE Public Access Plan, this document represents the authors' peer-reviewed, accepted manuscript.
The published version of the article is available from the relevant publisher.

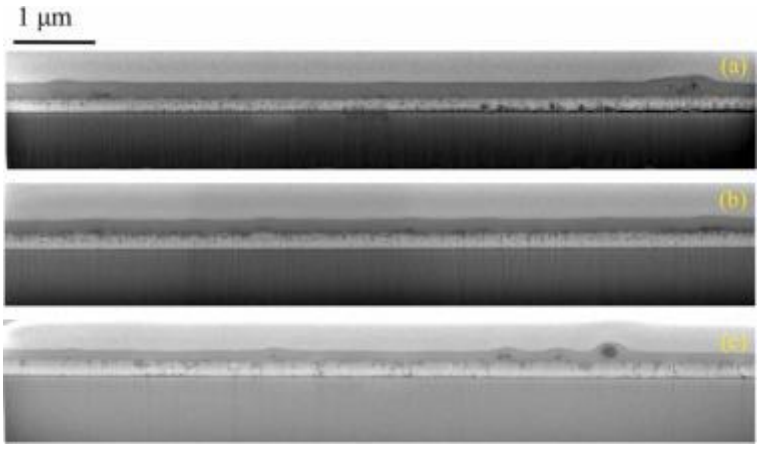

Fig. 6. Comparison of cross sections morphology among corroded samples with different grain size: (a) Grain size = 16.7 nm; (b) Grain size = 37.5 nm; (c) Grain size = 136.4 nm.

3.2.2. Elemental analysis by EDS

EDS mapping and spectrum analysis are conducted to better understand the corrosion behavior by measuring the compositions and elemental distribution of the corroded sample.

The SEM scanned surface of the corroded sample with grain size of 16.7 nm is shown in Fig. 7a. A number of white dots are distributed upon the surface. The yellow rectangle, which incorporates one whole white dot and other dark and grey features, is chosen as the representative region for the EDS analysis. The enlarged image of the yellow rectangle is displayed in 7b. Three representative zones marked by the red dashed squares are picked for three separate EDS mappings and spectra analysis.

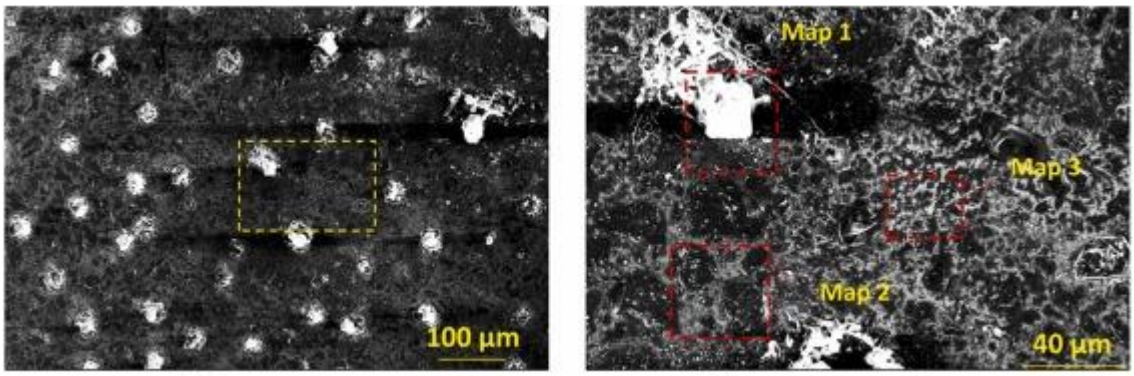

(a) SEM Image. (b) Three Regions for EDS.

Fig. 7. SEM image of corroded surface and three picked regions for EDS mappings (Grain: 16.7 nm; Corrosion: 600 °C, 30 min).

Fig. 8 illustrates the mappings results with each row displaying the spatial distribution of the detected elements in the corresponding zone. Each row shares the same scale bar as shown in the Ni map. The last picture at each row is the corresponding SEM image of this zone. The first row indicates that all three metal ingredients (K, Mg, and Na) and Cl from salts can be found in

Pursuant to the DOE Public Access Plan, this document represents the authors' peer-reviewed, accepted manuscript. The published version of the article is available from the relevant publisher.

the shiny area: potassium concentrates in the middle square area, which is surrounded by magnesium; sodium can be only observed in the top small area. The amounts of Ni, Cr and Mo in the white dot are very limited. The second and third rows show that the dark area contains more Mg and Cl.

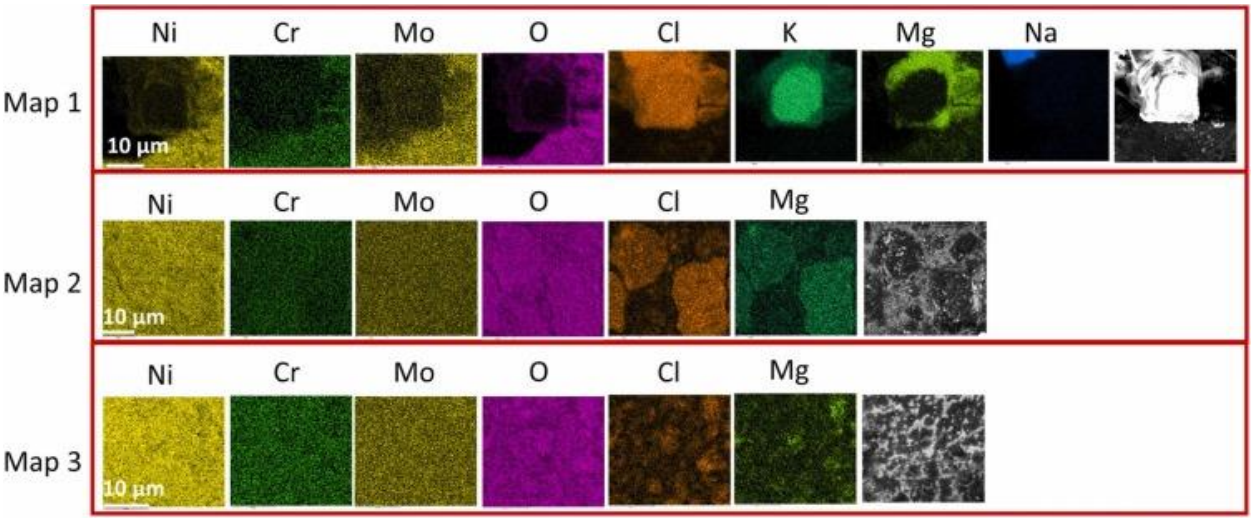

Fig. 8. EDS mapping results for three zones in Fig. 7b (Grain: 16.7 nm; Corrosion: 600 °C, 30 min).

Figs. 9 and 10 displays the results of corroded film with grain size of 37.5 nm. Compared with the corroded film deposited at room temperature (Grain size: 16.7 nm) as shown in Figs. 7 and 8, there are no white dots appearing on the surface, which instead displays mainly two types of structures: light smooth and dark rough areas. We picked the representative region in the yellow rectangle which contains both types of structures for further EDS analysis. EDS results indicate that the small light dots contain Mg and the dark region consists of more oxygen. and consequently no elements of K and Na detected in the film.

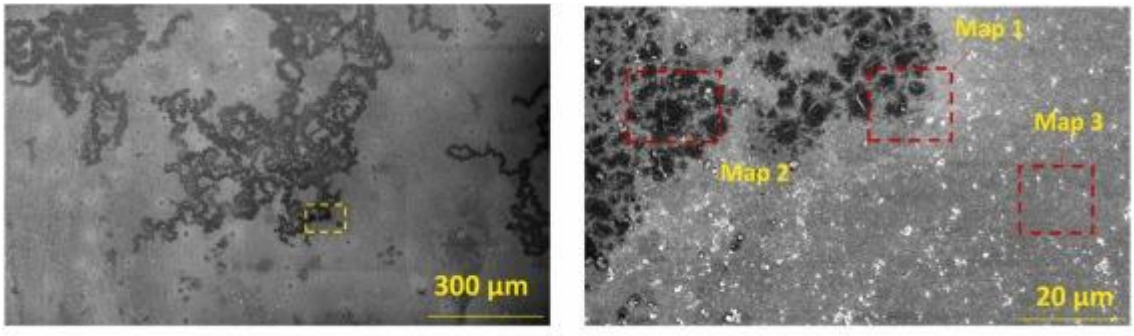

(a) SEM image. (b) Three regions for EDS.

Fig. 9. SEM image of corroded surface and three picked regions for EDS mappings (Grain size: 37.5 nm; Deposition: 150 °C, ~ 240 nm; Corrosion: 600 °C, 30 min).

Pursuant to the DOE Public Access Plan, this document represents the authors' peer-reviewed, accepted manuscript. The published version of the article is available from the relevant publisher.

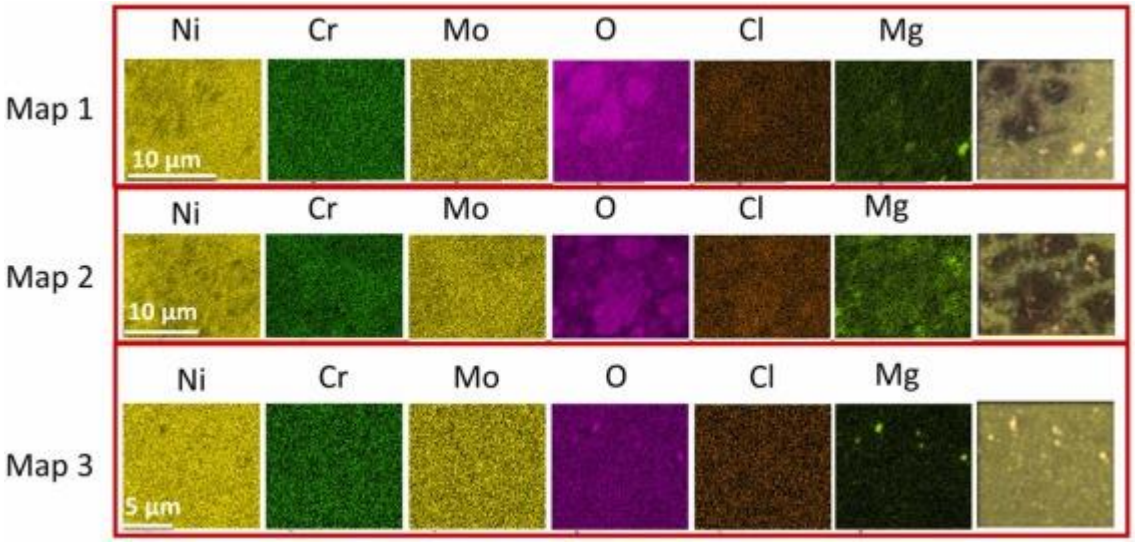

Fig. 10. EDS mapping results for the three zones in Fig. 9b (Grain size: 37.5 nm; Deposition: 150 °C, ~ 240 nm; Corrosion: 600 °C, 30 min).

The SEM and EDS results for the sample with largest grain size (136.4 nm) are demonstrated in Figs. 11 and 12 respectively. Again the surface displays two similar structures as film with grain size of 37.5 nm. There exists severe Chromium depletion in the dark oxidation areas. Cr depletion also occurs in the third region, accompanied with Mo enrichment. The second region displays minor corrosion with very limited amount of Mg and Cl detected.

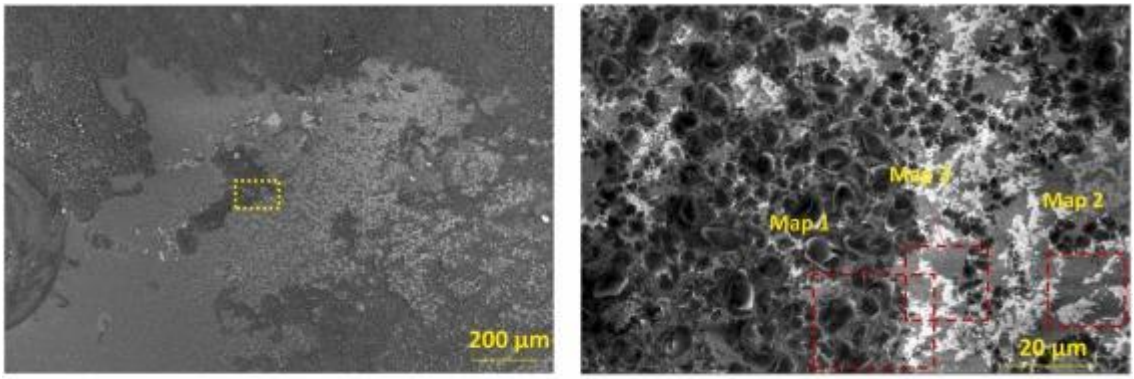

(a) SEM image. (b) Three regions for EDS.

Fig. 11. SEM image of corroded surface and three picked regions for EDS mappings (Grain size: 136.4 nm; Deposition: 600 °C, ~ 240 nm; Corrosion: 600 °C, 30 min).

Pursuant to the DOE Public Access Plan, this document represents the authors' peer-reviewed, accepted manuscript. The published version of the article is available from the relevant publisher.

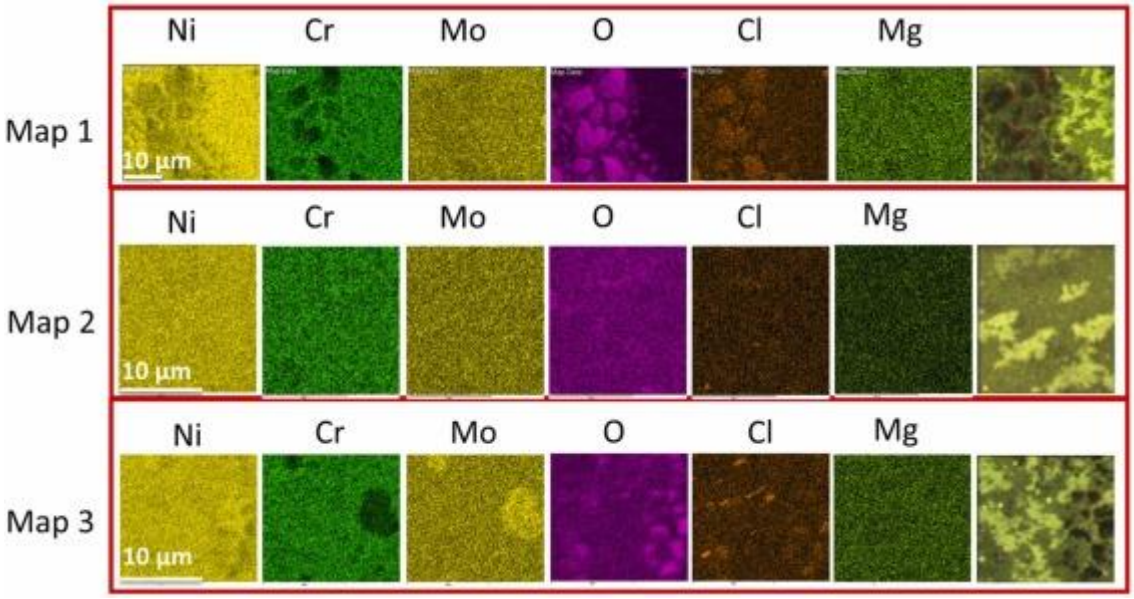

Fig. 12. EDS mapping results for the three zones in Fig. 11b (Grain size: 136.4 nm; Deposition: 600 °C, ~ 240 nm; Corrosion: 600 °C, 30 min).

The surface morphology and composition analysis results for the corroded sample at 550 ° are illustrated in Figs. 13 and 14 respectively. Unlike the corroded sample at high temperature, there is no large oxidation area found on this specimen. EDS mapping only found three main elements in Inconel 625 film without attack from salt elements such as Mg and Cl. These results indicate that corrosion effect drops dramatically at lower temperature although there still exists minor Cr depletion accompanied with Ni and Mo enrichment.

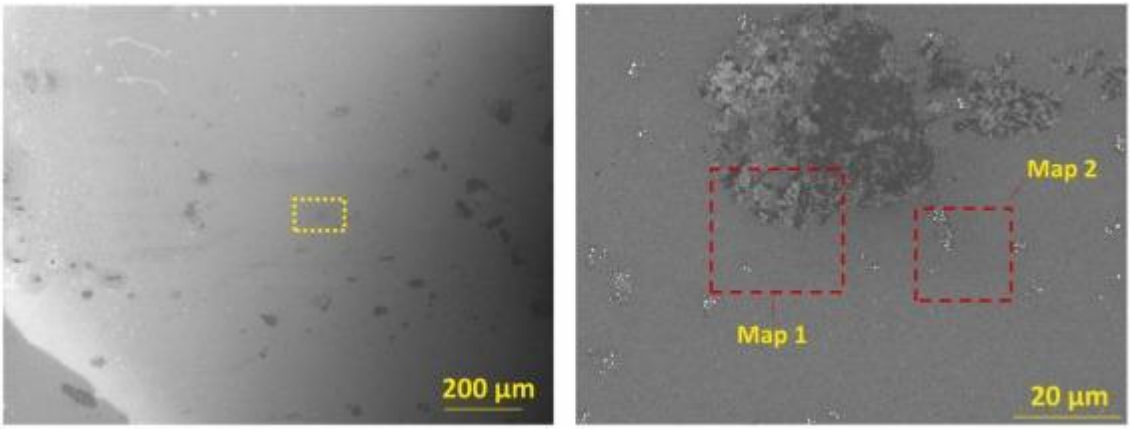

(a) SEM image. (b) Three regions for EDS.

Fig. 13. SEM image of corroded surface and three picked regions for EDS mappings (Grain size: 136.4 nm; Deposition: 600 °C, ~ 240 nm; Corrosion: 550 °C, 30 min).

Pursuant to the DOE Public Access Plan, this document represents the authors' peer-reviewed, accepted manuscript. The published version of the article is available from the relevant publisher.

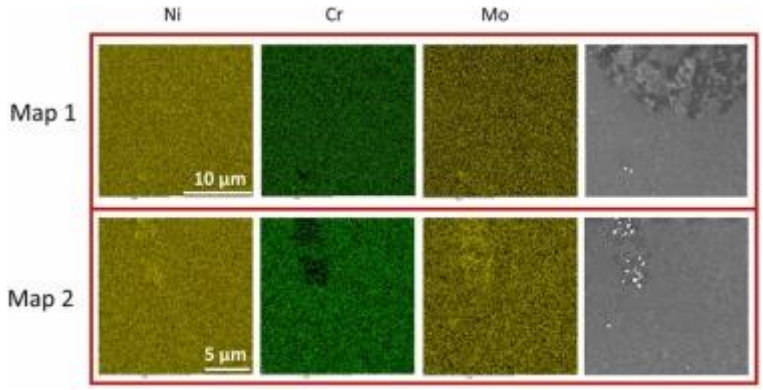

Fig. 14. EDS mapping results for the two zones in Fig. 13b (Grain size: 136.4 nm; Deposition: 600 °C, ~ 240 nm; Corrosion: 550 °C, 30 min).

Figs. 15 and 16 displays the corroded sample after 30 min corrosion at temperature of 650 °C. There are small white dots distributed upon the non-oxidation area. These white dots are found to be rich in magnesium and oxygen, while depleted in nickel and chromium. There is no obvious Mo and Ni enrichment occurring in this specimen found.

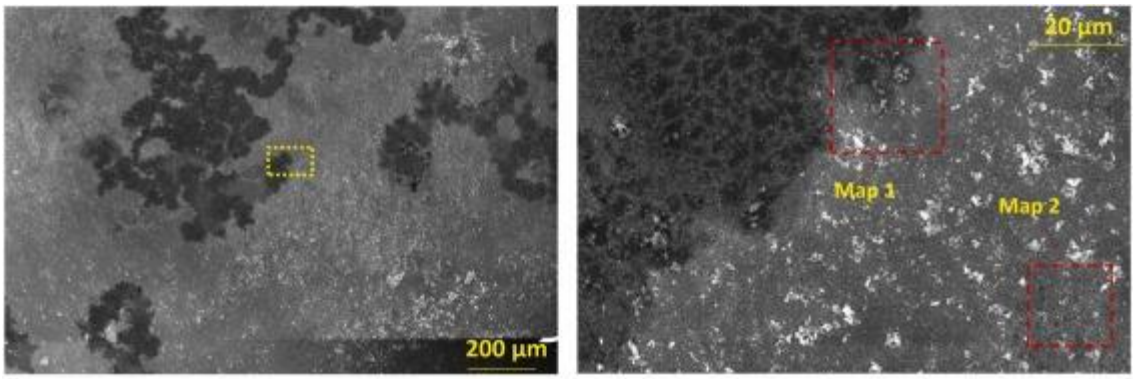

(a) SEM image. (b) Three regions for EDS.

Fig. 15. SEM image of corroded surface and three picked regions for EDS mappings (Grain size: 136.4 nm; Deposition: 600 °C, ~ 240 nm; Corrosion: 650 °C, 30 min).

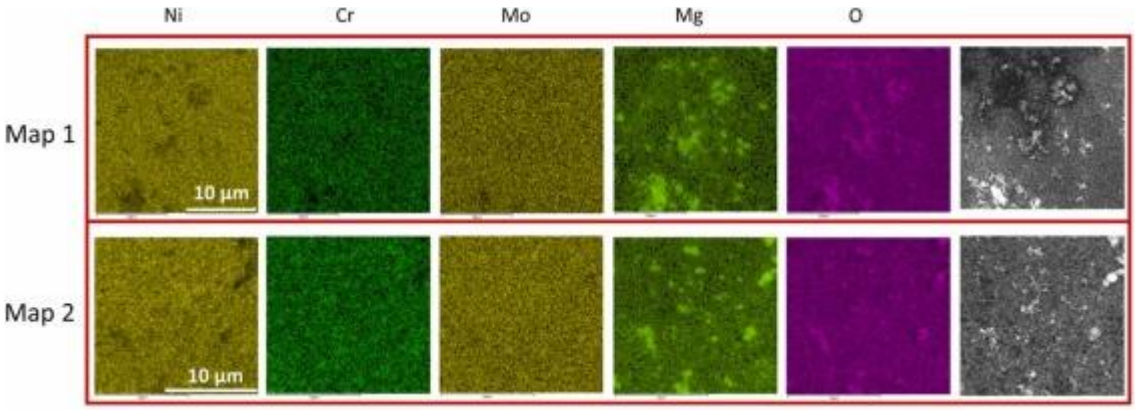

Pursuant to the DOE Public Access Plan, this document represents the authors' peer-reviewed, accepted manuscript. The published version of the article is available from the relevant publisher.

Fig. 16. EDS mapping results for the two zones in Fig. 15b (Grain size: 136.4 nm; Deposition: 600 °C, ~ 240 nm; Corrosion: 650 °C, 30 min).

The corrosion-induced content changes of the three main elements (Ni, Cr, Mo) in Inconel 625 calculated from EDS results above (Figs. 8, 10, 12, 14, and 16) is summarized and compared in Table 2, which indicates that chromium is more readily attacked by the molten salt than nickel and molybdenum. The composition of sample with larger grain size and lower corrosion temperature tends to be more close to that of original film.

Table 2. Change of the three main metal elements composition with grain size and corrosion temperature (atomic %, normalized by the total composition of the three elements in the film).

Element	Ni	Cr	Mo
Film w/o corrosion	67.0%	26.2%	4.8%
Grain size: 16.7 nm Corrosion: 600°C	82.3%	7.4%	10.3%
Grain size: 37.5 nm Corrosion: 600°C	81.0%	9.1%	9.9%
Grain size: 136.4 nm Corrosion: 600°C	77.8%	14.3%	7.9%
Grain size: 136.4 nm Corrosion: 550°C	72.0%	20.2%	6.9%
Grain size: 136.4 nm Corrosion: 650°C	78.3%	13.8%	8.0%

4. Discussion

4.1. Oxide layer

As demonstrated in 3.1.3, we didn't observe the oxide layer for the three films with larger grain size, while the thickness of oxide layer (NiO) with grain size of 37.5 nm and 16.7 nm are increased to 1.6 nm and 2.3 nm respectively. Based on the corrosion test results, these passive films provide limited protection against corrosion, which is not significant enough to compensate the negative effect of increased grain boundary density (more initiation sites). The reasons are twofold: (1) The thickness of the oxide layer is limited (~ 2 nm); (2) The main component of the oxide is NiO which is less corrosion resistant compared to Cr_2O_3 [23]. Ferguson et al. [24] found that the type and structure of the surface oxide layers is closely related to the oxidation temperature. NiO and Cr_2O_3 grow simultaneously on the surface of Inconel 625. NiO is predominate at lower temperature while the oxide film consists of almost entirely Cr_2O_3 at higher temperature (between 1073 and 1323 K) [25]. In our study, only NiO layer is identified on the surface because of low oxidation temperature.

Pursuant to the DOE Public Access Plan, this document represents the authors' peer-reviewed, accepted manuscript. The published version of the article is available from the relevant publisher.

4.2. Depletion and enrichment of metal elements

4.2.1. Cr depletion

The second columns of Figs. 8, 10, 12, 14, and 16 and Table 2 demonstrate the spatial distribution and composition of Cr in the films with different grain size or at different corrosion temperature, which shows Cr is the most readily attacked ingredient among the three main metal elements (Ni, Cr, and Mo) in the Inconel 625 film. The preferential leaching of Cr is consistent with other researchers' work [26], [27], [28], [29]. Cr-depletion holes can be observed from the corroded samples with grain size of 136.4 nm, but can not be clearly seen in the mappings of the films with grain size of 16.7 nm and 37.5 nm. One possible reason lies in the existence of a large quantity of small size Cr-depletion zones which may not be distinguished by EDS (spatial resolution ≥1μm). Another possible reason is that there is not enough Cr left in the corroded films for smaller grain size to be detected as Table 2 lists. Table 2 indicates that Cr depletion severely increases with the falling grain size. The main mechanism behind this phenomenon may be due to the uneven Cr distribution. For Ni-Cr-Mo alloys, the Cr-rich carbide tends to form in the interdendritic and solidification grain boundary regions [8]. To better illustrate the uneven distribution, we developed a python program to simulate the grain boundary by Voronoi diagram following the procedures below: (i) Randomly create seeds on the board with a given density; (ii) Create Voronoi diagram using python scipy.spatial Voronoi module; (iii) Locate cells on the voronoi ridge and fill it with grain boundary materials. Seeds in voronoi can be approximated as the number of grains. Given that the area of the board is 250nm × 250nm, grain size can be approximated as $\sqrt{625000}/\text{seeds}$. Three Voronoi fillings with different seeds are displayed in Fig. 17. The grain boundary density increases with the decreasing grain size, which leads to the fall of the Cr content in the grains (A portion of Cr in the grain diffuse to the boundary). As a result, more chromium is distributed to the grain boundary areas with the descending grain size. As mentioned before, grain boundary regions are more susceptible to corrosion and thus there is more Cr depletion for the alloy which possesses higher grain boundary density.

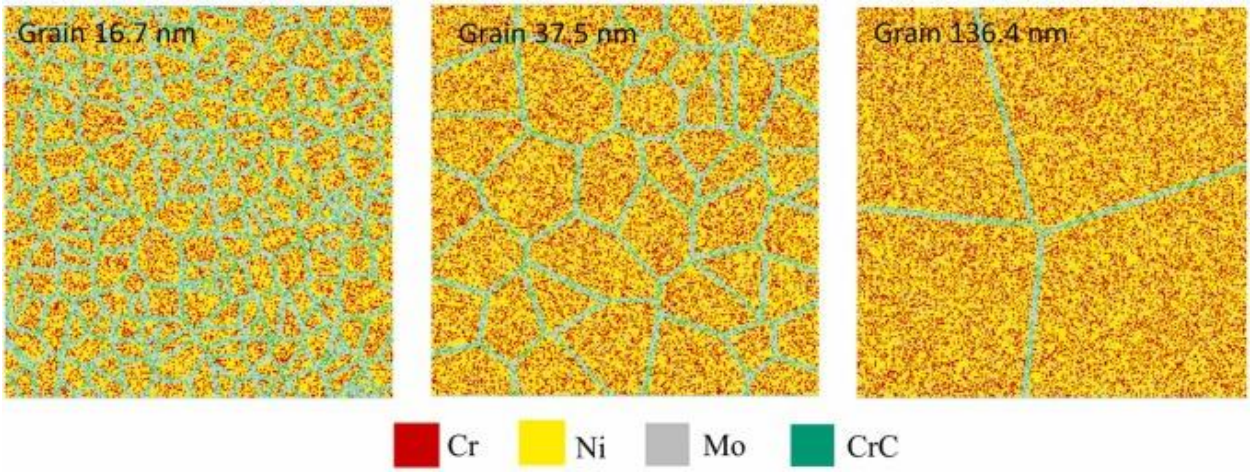

Fig. 17. Voronoi grain boundary illustration for different grain size.

Pursuant to the DOE Public Access Plan, this document represents the authors' peer-reviewed, accepted manuscript.
The published version of the article is available from the relevant publisher.

4.2.2. Mo and Ni enrichment

Molybdenum and Nickel enrichments occur in Cr-depleted holes as displayed in zone 3 in Fig. 12, and zone 2 in Fig. 14. In some cases, Cr-depleted regions overlap with Ni-depleted regions, as shown in zone 1 in Fig. 12, zones 1 and 2 in Fig. 16. This may be attributed by the different Gibbs free energy of the formation of the corresponding chlorides of these three elements [26]: ($CrCl_2$, −276 kJ/mol), ($NiCl_2$, −159.7 kJ/mol), ($MoCl_2$, −143.8 kJ/mol). Thus Mo is the least likely attacked element due to its lowest negative Gibbs free energy of $MoCl_2$ formation. Mo can diffuse to the surrounding area where large amount of Cr is depleted and form the Mo enrichment region. Ni is at some level between Mo and Cr. In the severely corroded areas, both Ni and Cr are attacked and show overlapping depletion. While in the minor corroded areas, only Cr is dissolved and Ni in the neighborhood can diffuse into these areas and form Ni-enrichment area.

4.3. Salt elements

Mg is the most commonly observed salt element among all the corroded films. It typically appears as small concentrated dots as shown in zones 1–3 in Fig. 10, zones 1 and 2 in Fig. 16. Oxygen and carbon are usually enriched in these shiny dots. The sample with smallest grain size exhibits large area Mg attack as shown in zones 1 and 2 of Fig. 8. But there are no shiny dots or large area of Mg found in samples with grain size of 136.4 nm at corrosion temperatures of 550 and 600 ° C as in Figs. 14 and 12. Those shiny dots form again at elevated temperature as shown in Fig. 16. Therefore, the amount of Mg incorporated in the film is an indicator of corrosion severity. Cl also appears in every corroded film except the one with minor corrosion at 550 °C. Cl accompanies Mg as displayed in zones 1, 2 and 3 in Fig. 8, and exists individually in zones 1 and 3 in Fig. 12. Na and K are only detected in the white shiny areas in the severely corroded sample with grain size of 16.7 nm as shown in Fig. 8.

4.4. Oxygen source

Oxygen can be detected in corroded films with all three grain sizes at all temperatures except the film with grain size of 136.4 nm at 550 °C as shown in Figs. 8, 10, 12, and 16. There are two potential oxygen sources: (i) surface oxidation of the film and (ii) oxygen residues in glove box. Based on our XRR analysis, oxidation is not detected in films with larger grain size. For smaller grain size, the very thin (~ 2 nm) oxidation layer should have limited contribution to EDS spectrum. Thus most oxygen should be incorporated into the film during the corrosion process. This may be a possible explanation why oxygen is not found in the most corrosion resistant sample at the lowest corrosion temperature (mildest corrosion).

4.5. Film detachment

Film detachment occurs readily for smaller grain size especially at high corrosion temperature as illustrated in Fig. 4. It is noteworthy that film adhesion may also play an important role in the peel-off. Previous studies [30], [31], [32] indicate that substrate temperature is an influencing

Pursuant to the DOE Public Access Plan, this document represents the authors' peer-reviewed, accepted manuscript.
The published version of the article is available from the relevant publisher.

factor on the film adhesion. Thus intergranular corrosion may not be the major contributing factor to the detachment of the film deposited at lower substrate temperature. Therefore, it is more reliable to compare the grain size effect among tests at lower corrosion temperature (550 and 600 °C) where peel-off is barely observed. Future study should be conducted to identify the contributing factor of film peel-off.

5. Conclusions

In this study, we explored the microstructure of the Inconel 625 film obtained by magnetron sputtering at different temperatures and then evaluated the grain size effect upon its corrosion behavior. The findings are concluded as follows:

(1) The SEM scan indicates that the grain size of the films obtained by magnetron sputtering grows from 16.7 nm to 136.4 nm when deposition temperature from 15 °C to 600 °C. XRD rocking curves indicate that film deposited at higher temperature has relatively higher degree of crystallinity.
(2) As ~ 2 nm thin NiO on the surface of the Inconel 625 film with smaller grain size is unable to compensate the negative effect of increased grain boundary density, the increase of the grain size improves the corrosion resistance of Inconel 625 against the MgCl2-NaCl-KCl molten salt.
(3) Films with all five grain size at all three corrosion temperatures display Cr depletion with different levels of severity. Cr is the most readily attacked element in the Inconel 625. Cr depletion can be alleviated by increasing the grain size. On the contrary, Mo is the least likely leached element for all five grain size studied and Mo enrichment occurs in most Cr-depleted regions as a result of Mo diffusion.
(4) Mg and Cl are two most seen salt elements in the corroded films. K and Na are only observed in the most severely corroded film with smallest grain size.

CRediT authorship contribution statement

Jinghua Feng: Investigation, Methodology, Software, Writing − original draft, Visualization. Li Mao: Investigation, Software, Validation, Formal analysis, Writing − review & editing. Guangcui Yuan: Methodology, Supervision. Youyang Zhao: Resources. Judith Vidal: Resources. Li (Emily) Liu: Funding acquisition, Supervision, Project administration.

Declaration of Competing Interest

The authors declare that they have no known competing financial interests or personal relationships that could have appeared to influence the work reported in this paper.

Acknowledgments

This material is based upon work supported by the U.S. Department of Energy's Office of Energy Efficiency and Renewable Energy (EERE) under the Generation 3 Concentrated Solar Power (CSP) Systems award number DE-EE0008380. This work was partially supported by

Pursuant to the DOE Public Access Plan, this document represents the authors' peer-reviewed, accepted manuscript. The published version of the article is available from the relevant publisher.

Nuclear Regulatory Commission under the contract NRC-HQ-84–15-G-0018. Certain commercial equipment, instruments, or materials (or suppliers, or software,.) are identified in this paper to foster understanding. The identification of any commercial product or trade name does not imply endorsement or recommendation by the National Institute of Standards and Technology, nor does it imply that the materials or equipment identified are necessarily the best available for the purpose. I am grateful to Dr. Robert Hull, Dr. Wei Ji, and Dr. Shanbin Shi for providing helpful advices and support on this work. I acknowledge use of facilities in the department of Materials Science and Engineering (MS&E) and the Center for Materials, Devices, and Integrated Systems (CMDIS) at Rensselaer Polytechnic Institute.

References

[1] J.P. Ram, T.S. Babu, N. Rajasekar. A comprehensive review on solar PV maximum power point tracking techniques. Renew. Sustain. Energy Rev., 67 (2017), pp. 826-847, 10.1016/j.rser.2016.09.076.

[2] L.A. Weinstein, J. Loomis, B. Bhatia, D.M. Bierman, E.N. Wang, G. Chen. Concentrating solar power. Chem. Rev., 115 (23) (2015), pp. 12797-12838, 10.1021/acs.chemrev.5b00397

[3] G.K. Singh. Solar power generation by PV (photovoltaic) technology: a review. Energy, 53 (2013), pp. 1-13, 10.1016/j.energy.2013.02.057

[4] Q. Wang, P. Chang, R. Bai, W. Liu, J. Dai, Y. Tang. Mitigation strategy for duck curve in high. Energies, 12 (3521) (2019)

[5] Becca Jones-Albertus, Confronting the Duck Curve: How to Address Over-Generation of Solar Energy. https://www.energy.gov/eere/articles/confronting-duck-curve-how-address-over-generation-solar-energy

[6] D. F. Williams, Assessment of candidate molten salt coolants for the NGNP/NHI heat-transfer loop, ORNL/TM-2006/69, Oak Ridge Natl. Lab. Oak Ridge, Tennessee (jun 2006).

[7] V. Shankar, K. Bhanu Sankara Rao, S. Mannan. Microstructure and mechanical properties of inconel 625 superalloy. J. Nucl. Mater., 288 (2) (2001), pp. 222-232, 10.1016/S0022-3115(00)00723-6

[8] J.C. Lippold, S.D. Kiser, J.N. DuPont. Welding Metallurgy and Weldability of Nickel-base Alloys

[9] M.J. Donachie, S.J. Donachie. Superalloys: A Technical Guide. ASM International (2002)

[10] W. Yu, D. Singh, D.M. France. Investigation of Corrosion of 304 Stainless, Inconel 625, and Haynes 230 in a Chloride-Salt-Based Thermal Storage Medium. J. Mater. Eng. Perform., 28 (12) (2019), pp. 7379-7389, 10.1007/s11665-019-04508-y

Pursuant to the DOE Public Access Plan, this document represents the authors' peer-reviewed, accepted manuscript. The published version of the article is available from the relevant publisher.

[11] D. Verdi, M.A. Garrido, C.J. Múnez, P. Poza. Cr3C2 incorporation into an Inconel 625 laser cladded coating: effects on matrix microstructure, mechanical properties and local scratch resistance. Mater. Des., 67 (2015), pp. 20-27

[12] P. Pragnya, D. Gall, R. Hull. In situ transmission electron microscopy of high-temperature Inconel-625 corrosion by molten chloride salts. J. Electrochem. Soc., 168 (5) (2021), p. 51507, 10.1149/1945-7111/ac0225

[13] J.C. Gomez-Vidal, A.G. Fernandez, R. Tirawat, C. Turchi, W. Huddleston. Corrosion resistance of alumina-forming alloys against molten chlorides for energy production. I: Pre-oxidation treatment and isothermal corrosion tests. Sol. Energy Mater. Sol. Cells, 166 (2017), pp. 222-233, 10.1016/j.solmat.2017.02.019

[14] N.P. Wasekar, N. Hebalkar, A. Jyothirmayi, B. Lavakumar, M. Ramakrishna, G. Sundararajan. Influence of pulse parameters on the mechanical properties and electrochemical corrosion behavior of electrodeposited Ni-W alloy coatings with high tungsten content. Corros. Sci., 165 (2020), Article 108409, 10.1016/j.corsci.2019.108409

[15] M.R. Zamanzad-Ghavidel, K. Raeissi, A. Saatchi. The effect of surface morphology on pitting corrosion resistance of Ni nanocrystalline coatings. Mater. Lett., 63 (21) (2009), pp. 1807-1809, 10.1016/j.matlet.2009.05.043

[16] V. Afshari, C. Dehghanian. Effects of grain size on the electrochemical corrosion behaviour of electrodeposited nanocrystalline Fe coatings in alkaline solution. Corros. Sci., 51 (8) (2009), pp. 1844-1849, 10.1016/j.corsci.2009.05.015

[17] L. Liu, Y. Li, F. Wang. Influence of grain size on the corrosion behavior of a Ni-based superalloy nanocrystalline coating in NaCl acidic solution. Electrochim. Acta, 53 (5) (2008), pp. 2453-2462, 10.1016/j.electacta.2007.10.048

[18] R. Ramanauskas, L. Gudavičiūtė, R. Juškėnas, O. Ščit. Structural and corrosion characterization of pulse plated nanocrystalline zinc coatings. Electrochim. Acta, 53 (4) (2007), pp. 1801-1810, 10.1016/j.electacta.2007.08.036

[19] E. Budke, J. Krempel-Hesse, H. Maidhof, H. Schüssler. Decorative hard coatings with improved corrosion resistance. Surf. Coat. Technol., 112 (1) (1999), pp. 108-113, 10.1016/S0257-8972(98)00791-9

[20] W.Y. Kwong, W.Y. Zhang. Electron-beam assisted platinum deposition as a protective layer for FIB and TEM applications. ISSM 2005 IEEE Int. Symp. Semicond. Manuf. Conf. Proc. (2005), pp. 469-471, 10.1109/Issm.2005.1513408

[21] X.L. Zhou, S.H. Chen. Theoretical foundation of X-ray and neutron reflectometry. Phys. Rep. -Rev. Sect. Phys. Lett., 257 (4–5) (1995), pp. 223-348, 10.1016/0370-1573(94)00110-O

Pursuant to the DOE Public Access Plan, this document represents the authors' peer-reviewed, accepted manuscript. The published version of the article is available from the relevant publisher.

[22] J. Feng, G. Yuan, L. Mao, J.B. Leão, R. Bedell, K. Ramic, E. de Stefanis, Y. Zhao, J. Vidal, L. Liu. Probing layered structure of Inconel 625 coatings prepared by magnetron sputtering. Surf. Coat. Technol., 405 (2021), Article 126545, 10.1016/j.surfcoat.2020.126545

[23] K. Sugimoto, M. Seto, S. Tanaka, N. Hara. Corrosion resistance of artificial passivation films of Fe2O3-Cr2O3-NiO formed by metalorganic chemical vapor deposition. J. Electrochem. Soc., 140 (6) (1993), p. 1586

[24] J.B. Ferguson, H.F. Lopez. Oxidation products of Inconel alloys 600 and 690 in pressurized water reactor environments and their role in intergranular stress corrosion cracking. Metall. Mater. Trans. A, 37 (8) (2006), pp. 2471-2479

[25] L. Kumar, R. Venkataramani, M. Sundararaman, P. Mukhopadhyay, S.P. Garg. Studies on the oxidation behavior of Inconel 625 between 873 and 1523 K. Oxid. Met., 45 (1–2) (1996), pp. 221-244, 10.1007/Bf01046827

[26] H. Sun, J. Wang, Z. Li, P. Zhang, X. Su. Corrosion behavior of 316SS and Ni-based alloys in a ternary NaCl-KCl-MgCl2 molten salt. Sol. Energy, 171 (2018), pp. 320-329

[27] H. Sun, P. Zhang, J.Q. Wang. Effects of alloying elements on the corrosion behavior of Ni-based alloys in molten NaCl-KCl-MgCl(2)salt at different temperatures. Corros. Sci., 143 (2018), pp. 187-199, 10.1016/j.corsci.2018.08.021

[28] B. Liu, X. Wei, W. Wang, J. Lu, J. Ding. Corrosion behavior of Ni-based alloys in molten NaCl-CaCl2-MgCl2 eutectic salt for concentrating solar power. Sol. Energy Mater. Sol. Cells, 170 (2017), pp. 77-86

[29] A. Ravi Shankar, K. Thyagarajan, U. Kamachi Mudali. Corrosion behavior of candidate materials in molten LiCl-KCl salt under argon atmosphere. Corrosion, 69 (7) (2013), pp. 655-665, 10.5006/0746

[30] I. Trakhtenberg, O.M. Bakunin, I.N. Korneyev, S.A. Plotnikov, A.P. Rubshtein, K. Uemura. Substrate surface temperature as a decisive parameter for diamond-like carbon film adhesion to polyethylene substrates. Diam. Relat. Mater., 9 (3) (2000), pp. 711-714, 10.1016/S0925-9635(99)00254-X

[31] V. Pershin, M. Lufitha, S. Chandra, J. Mostaghimi. Effect of substrate temperature on adhesion strength of plasma-sprayed nickel coatings. J. Therm. Spray. Technol., 12 (3) (2003), pp. 370-376, 10.1361/105996303770348249

[32] S.K. Mishra, A.S. Bhattacharyya. Effect of substrate temperature on the adhesion properties of magnetron sputtered nano-composite Si-C-N hard thin films. Mater. Lett., 62 (3) (2008), pp. 398-402, 10.1016/j.matlet.2007.05.043

Pursuant to the DOE Public Access Plan, this document represents the authors' peer-reviewed, accepted manuscript. The published version of the article is available from the relevant publisher.